fluids

MDPI

Article

Submesoscale Dynamics in the Gulf of Aden and the Gulf of Oman

Mathieu Morvan [1,*,†], **Xavier Carton** [1,*,†], **Stéphanie Corréard** [2,‡] **and Rémy Baraille** [2,‡]

[1] LOPS, Univ. Brest-CNRS-IFREMER-IRD, IUEM, Rue Dumont d'Urville, 29280 Plouzané, France
[2] SHOM/DOPS/STM/DTO, Météopole, 42 Avenue Gaspard Coriolis, 31100 Toulouse Cedex 5, France; stephanie.correard@shom.fr (S.C.); remy.baraille@shom.fr (R.B.)
* Correspondence: mathieu.morvan@univ-brest.fr (M.M.); xavier.carton@univ-brest.fr (X.C.)
† Current adress: IUEM, Rue Dumont d'Urville, 29280 Plouzané, France
‡ Current adress: Météopole, 42 Avenue Gaspard Coriolis, 31100 Toulouse Cedex 5, France

Received: 6 July 2020; Accepted: 25 August 2020 ; Published: 28 August 2020

Abstract: We have investigated the surface and subsurface submesoscale dynamics in the Gulf of Aden and the Gulf of Oman. Our results are based on the analyses of regional numerical simulations performed with a primitive equation model (HYCOM) at submesoscale permitting horizontal resolution. A model zoom for each gulf was embedded in a regional mesoscale-resolving simulation. In the Gulf of Aden and the Gulf of Oman, the interactions of mesoscale structures and fronts instabilities form submesoscale eddies and filaments. Rotational energy spectra show that the Gulf of Aden has a higher ratio of submesoscale to mesocale energy than the Gulf of Oman. Fast waves (internal gravity waves, tidal waves, Kelvin waves) and slow waves (Rossby waves) were characterized via energy spectra of the divergent velocity. Local upwelling systems which shed cold filaments, coastal current instabilities at the surface, and baroclinic instability at capes in subsurface were identified as generators of submesocale structures. In particular, the Ras al Hamra and Ras al Hadd capes in the Gulf of Oman, and the Cape of Berbera in the Gulf of Aden, are loci of submesoscale eddy generation. To determine the instability mechanisms involved in these generations, we diagnosed the Ertel potential vorticity and the energy conversion terms: the horizontal and vertical Reynolds stresses and the vertical buoyancy flux. Finally, the impacts of the subsurface submesoscale eddy production at capes on the diffusion and fate of the Red Sea Water (in the Gulf of Aden) and the Persian Gulf Water (in the Gulf of Oman) are highlighted.

Keywords: submesoscale instabilities; eddies and waves; upwelling fronts

---

1. Introduction

The Gulf of Oman and the Gulf of Aden, located on the western side of the Arabian Sea, are two semi enclosed basins receiving the warm and salty waters produced respectively in the Persian Gulf and the Red Sea, namely, PGW and RSW (Persian Gulf Water and Red Sea Water) [1]. PGW and RSW enter the Gulf of Oman and the Gulf of Aden via the Strait of Hormuz and the Strait of Bab el Mandeb. They cascade over the sloping topography down to their neutral buoyancy 252.2 level. PGW and RSW settle at 250–300 and 600–1000 m depths respectively [2,3].

The fate of PGW and RSW is governed by the deep-reaching influence of surface mesoscale eddies with radii 50–100 km [4,5]. The dynamical influence of these eddies can reach 1000 m depth. Mesoscale eddies can interact with each other, or become unstable, subsequently forming smaller-scale structures [6,7]. In the Gulf of Aden, alternatively signed mesoscale eddies propagate westward at the speed of the long Rossby waves [8] all through the year. In the Gulf of Oman, a mesoscale dipole has been observed in spring near the Cape of Ra's al Hamra [9]. PGW and RSW spread into the Gulf of Oman and the Gulf of Aden at intermediate depths under the influence of these mesoscale eddies. These outflows form filaments which eventually break into submesoscale eddies $[\mathcal{O}(0.1\text{–}20)\ \text{km}]$ (i.e., eddies with radii smaller than the deformation radius). The estimates of the deformation radii (R_d) from [10] are about 40 and 50 km in the Gulf of Oman and the Gulf of Aden respectively (see [11,12]). Submesoscale eddies have been observed and sampled in the oceans for decades: Meddies in the Western Atlantic ocean [13], small-scale and intense vortices in the Beaufort Gyre [14], submesoscale coherent vortices in the north-western Mediterranean Sea [15], Cuddies in the Carlifornia Current System [16], and submesoscale coherent vortices in the Gulf Stream [17]. In the Arabian Sea, submesoscale eddies have been observed much less frequently. A submesoscale eddy, containing PGW, was observed off the southern Omani coast in spring 2011 by [18]. Previously, deep and small eddies of RSW were sampled in the eastern Arabian Sea [19,20]. Recently, a submesoscale cyclone of RSW was observed and reported by [21].

Mesoscale eddies can generate submesoscale eddies via frontal instabilities [22–24]. Submesoscale eddies can also originate from the interaction of mesoscale eddies with the sloping topography through the bottom boundary layer [11,25–27]. Baroclinic instability of the bottom density current of outflow water flowing over the sloping topography can generate submesoscale eddies [28]. The Rossby number of such submesoscale eddies is usually not small [29].

In this paper, we investigate the submesoscale dynamics in the Gulf of Oman and the Gulf of Aden by analysing regional numerical simulations performed with a primitive equations model at submesoscale resolution. At the surface, a substantial part of the kinetic energy is induced by the mesoscale and submesoscale eddies. Internal-gravity waves and tides are also generated in both gulfs, mostly counting in the non-balanced part of the flow in the super-inertial and submesoscale range. Baroclinic, horizontal shear, and frontal instabilities generate surface submesoscale eddies. Depending on the generation mechanism, submesoscale eddies lie at the surface or at depth. Submesoscale eddies are also found below the pycnocline at intermediate depths, evolving the fate of PGW and RSW.

The paper is organized as follows: the model set-up and methods are described in Section 2, the results are shown in Section 3, and the conclusions are drawn in Section 4.

2. Model Set-Up and Methods

2.1. Model Set-Up

We performed regional realistic numerical simulations with the HYbrid Coordinate Ocean Model (HYCOM, [30]), with local zooms. Local zooms are 1-way nest integrations based on the Agrif method [31]. The parent simulation solved the primitive equations' mesoscale resolution (about 5 km on the horizontal). The parent domain covered the Arabian Sea and the evaporation basins, viz, the Red Sea and the Persian Gulf, as shown in Figure 1a. The initialization and surface and boundary forcings used in the parent simulation are described in [32]. Then, two Agrif zooms were performed at submesoscale resolution (about 1.5 km on the horizontal) over the Red Sea and the Gulf of Aden on the one hand (see Figure 1b), and the Gulf of Oman on the other hand (see Figure 1c). Both Agrif zoomed simulations were run over the year 2011. The baroclinic and barotropic time steps were respectively 40 and 1 s. The two-dimensional surface data were saved hourly, while the three-dimensional data from surface to bottom, were saved daily. In the vertical dimension, 40 levels were used. They were distributed as follows: 20 levels in z-coordinates discretized the upper layer from the surface to 100 m depth; below, 20 levels in isopycnic coordinates sampled the rest of the water column (see [32] for details). The ocean surface was forced with re-analyses of hourly atmospheric forcing from the French meteorological office (Météo France) at 0.25° × 0.25° resolution. The boundaries were forced by the parent simulation including tides from TOPEX data (8 tide modes). The vertical mixing was parameterized with a KPP-scheme [33]. Model viscosity was kept to a minimum compatible with numerical stability.

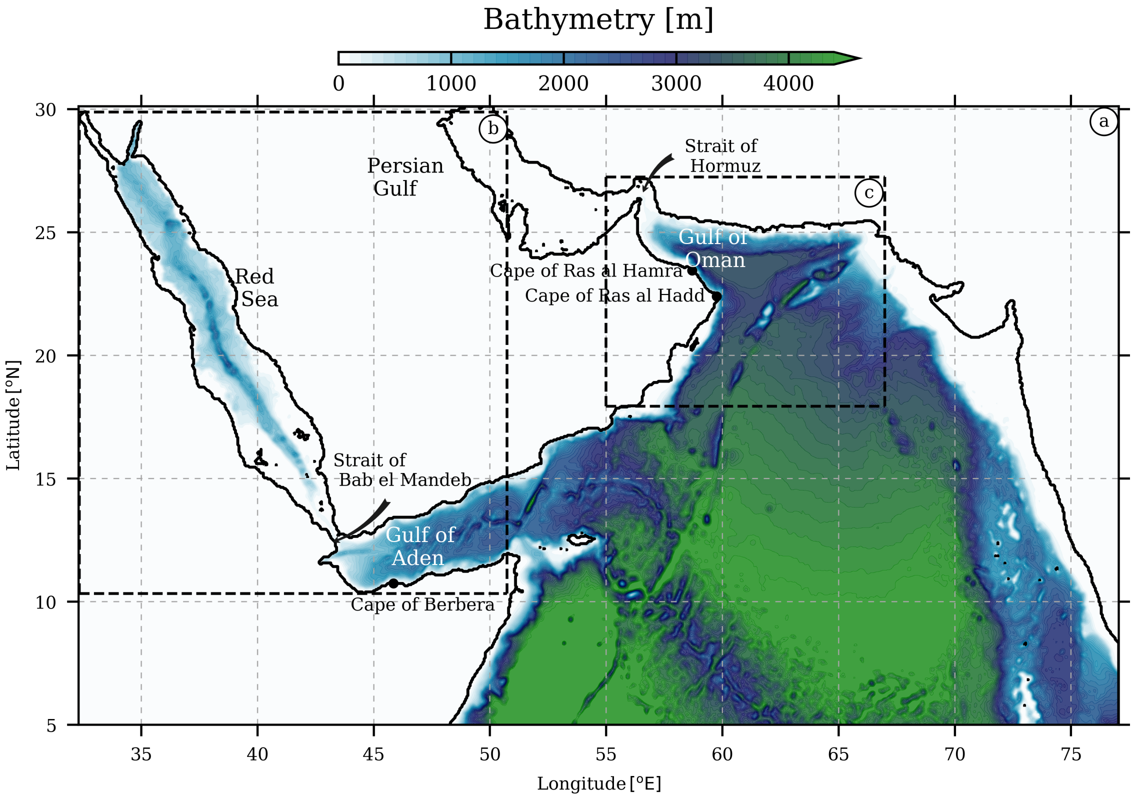

Figure 1. Bathymetry of the Arabian Sea (**a**). The domains used for the two AGRIF zooms are displayed in dashed black lines (**b**,**c**).

2.2. Methods

We highlight the presence of submesoscale structures as eddies, filaments, and fronts by diagnosing the vertical relative vorticity:

$$\zeta = \boldsymbol{\nabla} \times \boldsymbol{u}\,, \tag{1}$$

with $\boldsymbol{u}$, the velocity vector. When normalized by the areal average of the Coriolis frequency (f_0) over the local domain, relative vorticity provides information on the dynamical regimes and force balances which govern the flow.

The Ertel potential vorticity (EPV) is also computed:

$$Q = (f + \zeta)\, \boldsymbol{z} \cdot \boldsymbol{\nabla} b\,, \tag{2}$$

with f the Coriolis frequency varying with latitudes, and b the buoyancy acceleration. The Ertel potential vorticity is conserved materially in the absence of forcing and of dissipation, and its horizontal integral between two isopycnals is conserved in the absence of diapycnal mixing, surface forcing, and lateral mixing at the boundaries (Haynes and McIntyre impermeability theorem [34]).

Flow instabilities were characterized by computing the energy conversions terms as defined in [35] as:

$$\mathrm{HRS} = -\overline{\boldsymbol{u}'v'} \cdot \partial_y \overline{\boldsymbol{u}} - \overline{\boldsymbol{u}'u'} \cdot \partial_x \overline{\boldsymbol{u}}\,; \tag{3}$$

$$\mathrm{VRS} = -\overline{\boldsymbol{u}'w'} \cdot \partial_z \overline{\boldsymbol{u}}\,; \tag{4}$$

$$\mathrm{VBF} = \overline{w'b'}\,; \tag{5}$$

where means a time average and $'$ the deviation from the time average. The horizontal and vertical Reynolds stresses (HRS and VRS) are related to the horizontal and vertical shear instabilities respectively. They transfer mean kinetics to eddy kinetic energy. The vertical buoyancy flux (VBF) indicates eddy potential to eddy kinetic energy conversions. It characterizes baroclinic instability.

3. Results

3.1. Surface Submesoscale Dynamics

At mesoscale resolution, regional numerical simulations have shown that the surface mesoscale circulation is dominated by eddies in the Gulf of Oman [36] and in the Gulf Aden [32]. By increasing the horizontal grid resolution up to submesoscales, the recurrent mesoscale dynamical structures and processes, for instance, the westward propagation of anticyclones in the Gulf of Aden, and the Ra's al Hadd jet at the mouth of the Gulf of Oman, were well reproduced. Furthermore, at high resolution, smaller structures, such as eddies and filaments, appeared with finite values of the dynamical Rossby numbers (ζ/f_0), as shown in Figure 2. Structures with the highest ζ/f_0 values arose as soon as mesoscale currents or eddies flowed close to the coast. For instance, during the winter monsoon, in the Gulf of Oman, at submesoscale, cyclonic eddies were formed at the cape of Ra's al Hamra and near the Cape of Ra's al Hadd (see Figure 2, 1st row, 1st column). During the summer monsoon an intense submesoscale anticyclonic eddy was located in the southeastern Gulf of Aden (see Figure 2, 2nd row, 3rd column). Filaments of intense relative vorticity were also observed at the surface. In the Gulf of Oman, during the summer monsoon a coastal cyclonic filament was located along the northern coast (see Figure 2, 1st row, 3rd column). During the fall intermonsoon, cyclonic filaments were also present in the center of the Gulf of Aden (see Figure 2, 2nd row, 4st column).

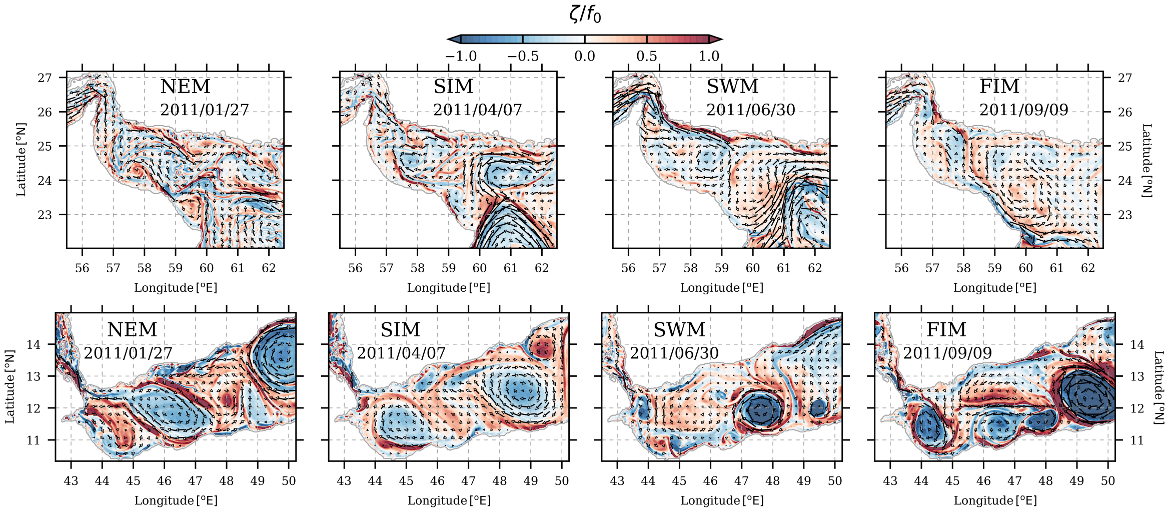

Figure 2. Snapshots of surface vertical relative vorticity normalized by the areal mean Coriolis frequency (f_0), (1st row) in the Gulf of Oman, and (2nd row) in the Gulf of Aden representative of the surface dynamics during (1st column) the North-East Monsoon (NEM), (2nd column) the Spring Inter-Monsoon (SIM), (3rd column) the South-Western Monsoon (SWM), and (4st column) the Fall Inter-Monsoon (FIM). Black arrows stand for the surface velocity vectors.

The Power Spectrum Densities (PSDs) of surface horizontal velocities highlight the seasonal variability of the submesoscale activity, as shown in Figure 3. A Hanning windowing function was applied in the real space before going through the spectral space. In the Gulf of Oman, the spectral slope is shallower between $R_d/2 \sim 20$ km and $R_d/10 \sim 4$ km corresponding to the submesoscale range. Indeed, the steep spectra are due to dominant mesoscale activity for scales longer than $R_d/2$, and due to viscous effects for scales shorter than $R_d/10$. The submesoscale energy amplitude is maximal during the North-East Monsoon (NEM) with a k^{-2} spectral slope. During the Spring Inter-Monsoon (SIM), the submesoscale spectral amplitude weakens and the slope by close to k^{-3}. The smaller submesoscale spectral amplitudes can be found during the South-West Monsoon (SWM) and the Fall Inter-Monsoon

(FIM) with slopes close to k^{-4}. During these periods, intense mesoscale eddies (at the scale of the Gulf of Aden or of the Gulf of Oman) dominate the regional flow. The k^{-2} slope indicates an active submesoscale activity during NEM in comparison with the other seasons [22]. During the NEM, the wind stress is not as strong as during the SWM, but mesoscale eddies are seldom present; the circulation is mostly cyclonic (and alongshore) at the scale of the Gulf.

In the Gulf of Aden, the spectral slopes seem to vary less in the submesoscale range (between $R_d/2 \sim 25\,\mathrm{km}$ and $R_d/10 \sim 5\,\mathrm{km}$), than in the Gulf of Oman. Note that they are also shallower in this range than in the mesoscale range, where they are close to k^{-4} whatever the season. In fact, there is more mesoscale energy in the Gulf of Aden. Indeed, all year long, the surface flow field of the Gulf of Aden is dominated by alternatively signed mesoscale eddies with diameters about 100–200 km, that is, half the gulf width to the full gulf width [32].

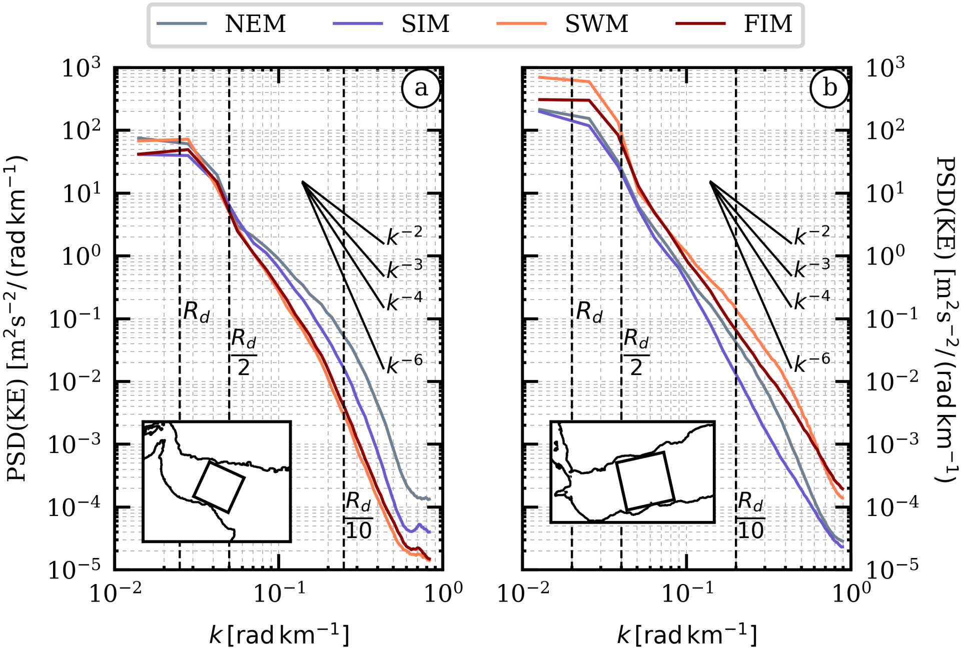

Figure 3. Power Spectrum Densities (PSDs) of horizontal surface velocities computed (**a**) in the Gulf of Oman, and (**b**) in the Gulf of Aden (see square boxes drawn in insets for the computional domains). PSDs are timely averaged for (gray) the North-East Monsoon (NEM), (blue) the Spring Inter-Monsoon (SIM), (orange) the South-West Monsoon (SWM), and (red) the Fall Inter-Monsoon (FIM). Solid black lines stand for benchmarks of power laws, and information about the deformation radii and wavelengths (i.e., R_d, $R_d/2$, and $R_d/10$) is indicated in dashed black lines.

At submesocale, many physical processes can occur. Eddies and filaments are balanced motions for their main velocity components; and they have non zero potential vorticity anomaly (with respect to the environment), contrary to internal, coastal (Kelvin), or internal inertial waves which either are imbalanced motions or have zero potential vorticity anomaly. Still, all these motions are reflected in the Sea Surface Height (SSH) variations. The SSH distributions in the two-dimensional space (k, ω) Fourier space are shown in Figure 4 for Figure 4a the Gulf of Oman and Figure 4c the Gulf of Aden with k the isotropic wave number and ω, the frequency. The SSH spectral signals are most energetic at mesoscale and submesoscale, and at low frequency in the Gulf of Oman and the Gulf of Aden. At higher frequency, the larger discontinuous amplitudes correspond essentially to flows forced by atmosphere ($\omega = \mathrm{day}^{-1}$) and the tide ($\omega = \mathrm{M2}$, the semi-diurnal tide) and its harmonics.

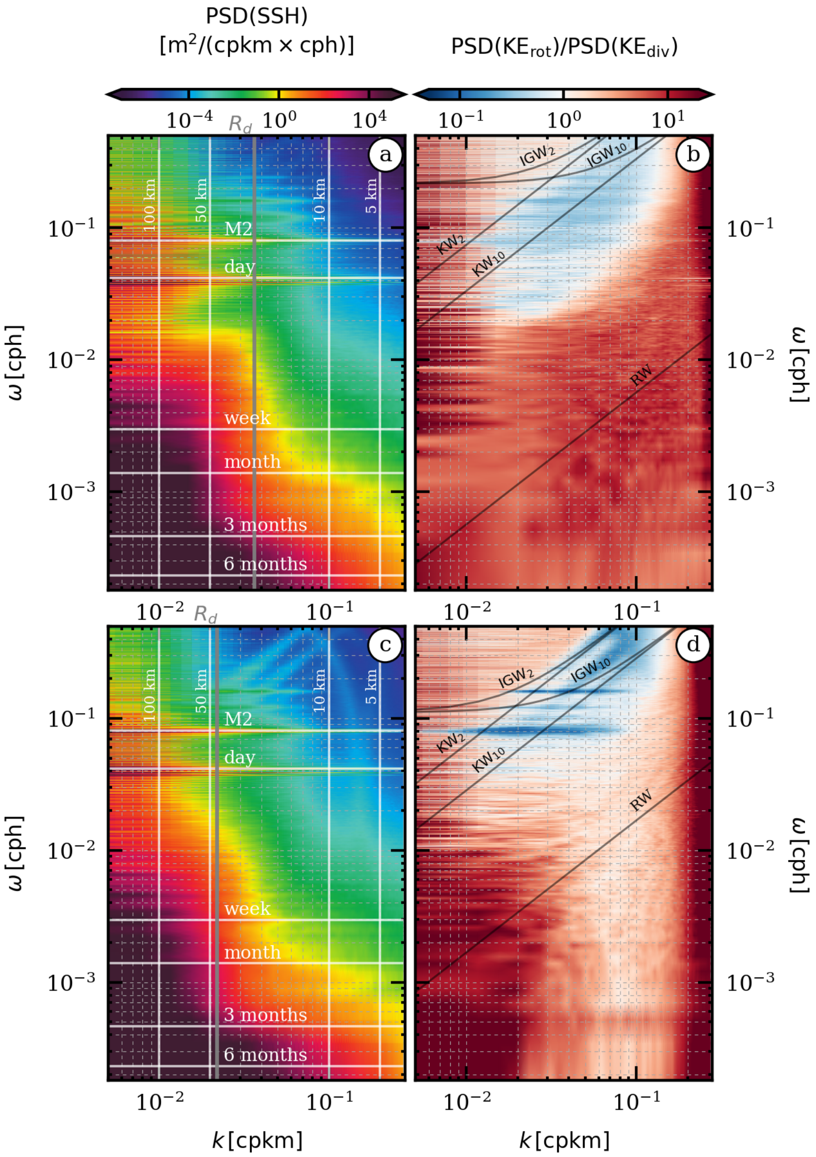

Figure 4. Power Spectrum Densities (PSD) of Sea Surface Height (SSH) computed (**a**) in the Gulf of Oman and (**c**) in the Gulf of Aden. The deformation radii (in gray) and benchmark wavelengths (in white) are indicated in vertical solid lines. Benchmark periods are indicated in horizontal white lines. Ratio of the PSD of the kinetic energy of the rotational part of the flow over the PSD of the kinetic energy of the divergent part computed (**b**) in the Gulf of Oman, and (**d**) in the Gulf of Aden. Dispersion relations of inertia-gravity waves of the second (IGW_2) and the tenth (IGW_{10}) modes of Kelvin Waves of the second (KW_2) and the tenth (KW_{10}) modes, and of Rossby Waves (RW), are drawn as solid black lines.

To determine the processes which dominate the submesoscale range, we decompose the flow in a rotational and a divergent parts (Helmholtz decomposition), as :

$$\boldsymbol{u} = \boldsymbol{u}_{\text{rot}} + \boldsymbol{u}_{\text{div}} = \boldsymbol{k} \times \boldsymbol{\nabla}\psi + \boldsymbol{\nabla}\chi\,. \tag{6}$$

Equation (6) was solved using a multigrid solver with Dirichlet boundary conditions. Reference [37] discussed the partitioning of the flow into balanced motions and internal gravity waves through this method. Their results indicate that this method is accurate in summer. In winter, it must be used with caution. However, the rotational part is related to the relative vorticity which is high in small eddies and in filaments which represent an important part of the submesoscale energy in the regions of interest. Indeed, vertical velocities are high in the submesoscale filaments, so that the divergent part represents in part the submesoscale filaments. However, the divergent part also characterizes gravity waves the evolution of which is based on the local convergence and divergence of water masses. We can identify these wave via their dispersion relations. The ratios of the PSD of surface horizontal rotational velocity over the PSD of surface horizontal divergent velocity are shown in Figure 4b for the Gulf of Oman and Figure 4d for the Gulf of Aden. Below $\omega = \mathrm{day}^{-1}$, the kinetic energy is mostly due to the rotational part of the flow (red patches). This is the signature of the mesoscale and submesoscale eddies as well as filaments. As shown in [32,36] the surface dynamics are dominated by mesoscale eddies. Furthermore, continuous blue rays in the submesoscale range indicate fast wave propagation ($\omega \geq \mathrm{day}^{-1}$). This is the signature of internal Kelvin waves whose dispersion relation is:

$$\omega_{KW_i} = \frac{NH}{2\pi i} k\,, \tag{7}$$

with N being the stratification frequency equal to $2.1 \times 10^{-3}\,\mathrm{s}^{-1}$ in the Gulf of Oman and $1.6 \times 10^{-3}\,\mathrm{s}^{-1}$ in the Gulf of Aden. H is the depth averaged over the computational domains about 2500 m in the Gulf of Oman and 2750 m in the Gulf of Aden. i is an integer representing the baroclinic mode considered. Our results indicate that in semi-enclosed basins such as the Gulf of Oman and the Gulf of Aden, Kelvin waves capture large parts of the energy in the submesoscale and high frequency ranges. In addition to [37,38] who worked on the open ocean region, this result can also be of great importance for the future space missions in order to characterize the ocean motions in coastal regions. The dispersion relation of inertia-gravity waves (IGW) are also indicated $\left(\omega_{\mathrm{IGW}} = \sqrt{\omega_{\mathrm{KW}}^2 + f_0^2}\right)$. Note that the magnitude of the PSD ratio dramatically increases at the finest scales due to aliasing.

3.2. Submesoscale Fronts from Coastal Upwelling

In the Gulf of Aden, during the SWM, the wind stress is favorable to upwelling at the northern coast. A sea surface temperature anomaly (with respect to a mean) is shown in Figure 5a. A negative temperature anomaly, in the form of a filament, was located in the western Gulf of Aden, extending offshore unto the center of the gulf. It splits into two branches under the influence of two anticyclonic eddies. This filament is associated with two submesoscale temperature fronts offshore, and it is connected to the upwelling front at the coast. The upwelling affects the first hundred meters of the ocean, vertically, as shown in Figure 5b. Even below the pycnocline, the density contours gradually tilt upwards. The submesoscale front is associated with large positive relative vorticity ($\zeta/f_0 \geq 1$), as shown in Figure 5c, which generates up- and downwelling via the ageostrophic circulation. The section of fQ (potential vorticity multiplied by Coriolis frequency) across the filament indicates a change in sign at both fronts (see Figure 5d) . $fQ < 0$ is a criterion for symmetric instability [39], in this case, confined in the surface mixed layer. Subsequent submesoscale eddies may be formed.

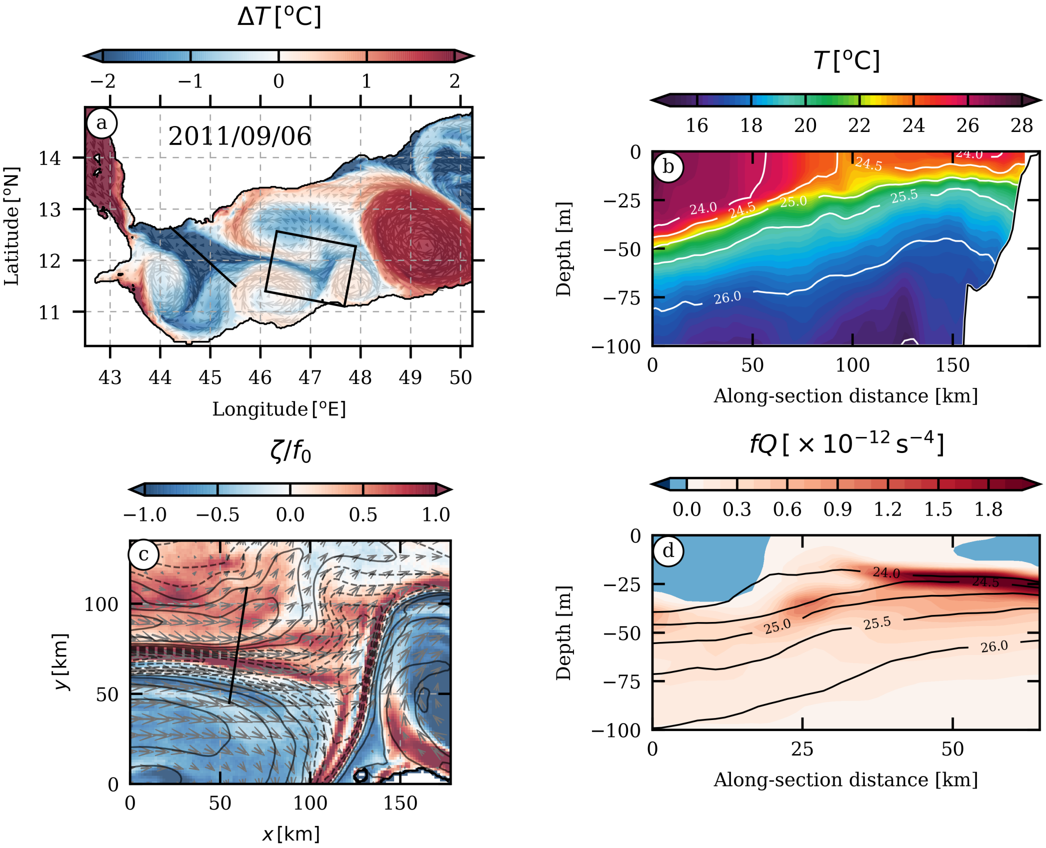

Figure 5. (**a**) Surface temperature anomaly in the Gulf of Aden. Arrows stand for the surface velocity vectors. (**b**) Vertical slice of temperature in the Gulf of Aden. The location of the section is drawn as a black solid line in (**a**). Density contours ($\mathrm{kg\,m^{-3}}$) are drawn as white solid lines. (**c**) Surface relative vorticity normalized by the aeral average of the Coriolis frequency (see black square box in (**a**) for location). Black contours stand for the surface temperature anomaly. Arrows stand for the surface velocity vectors. (**d**) Vertical slice of PV.Density contours ($\mathrm{kg\,m^{-3}}$) are drawn as black solid lines.

In the same manner, a submesoscale cold filament is located in the western Gulf of Oman along the northern coast (see Figure 6a). The vertical cross-filament section (see Figure 6b) indicates that an upwelling process affecting the first hundred meters depth is at play. The sharp coastal density gradient is associated with high relative vorticity value (see Figure 6c). As in the Gulf of Aden, the potential vorticity multiplied by the Coriolis frequency changes sign at the two sides of the front (see Figure 6d), again indicating a possible centrifugal instability in the surface mixed layer. The subsequent generation of submesoscale eddies might be captured with a higher horizontal resolution model configuration.

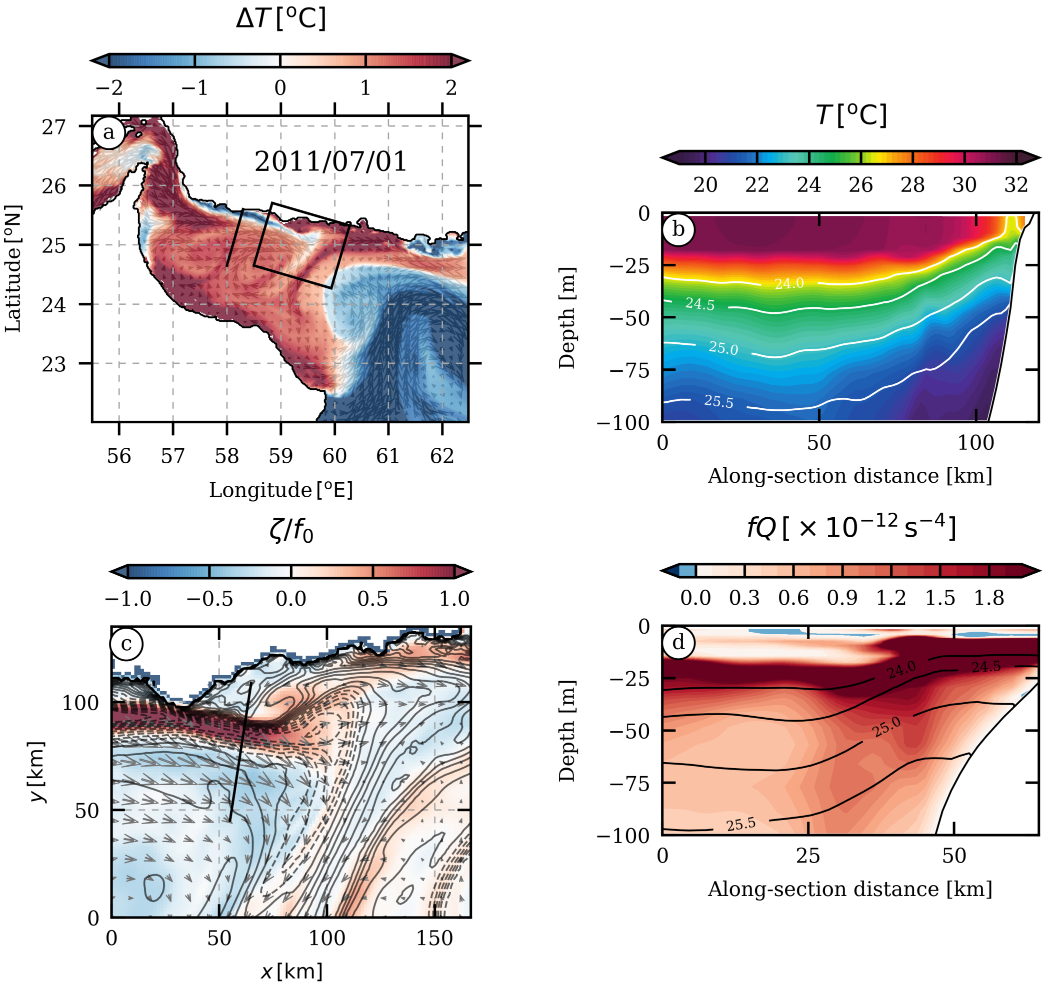

Figure 6. (**a**) Surface temperature anomaly in the Gulf of Oman. Arrows stand for the surface velocity vectors. (**b**) Vertical slice of temperature in the Gulf of Oman. The location of the section is drawn as a black solid line in (**a**). Density contours ($\mathrm{kg\,m^{-3}}$) are drawn as white solid lines. (**c**) Surface relative vorticity normalized by the areal average of the Coriolis frequency (see black square box in (**a**) for location). Black contours stand for the surface temperature anomaly. Arrows stand for the surface velocity vectors. (**d**) Vertical slice of PV. Density contours ($\mathrm{kg\,m^{-3}}$) are drawn as black solid lines.

3.3. Coastal Submesoscale Eddies

As mentioned in the Section 3.1, an intense submesoscale anticyclone is located in the eastern Gulf of Aden along the southern coast. A snapshot of the relative vorticity normalized by the areal average of the Coriolis frequency is shown in Figure 7a. The submesoscale eddy under consideration is located in the square box. To gain insight about its formation, we computed the energy conversions (HRS, VRS, and VBF) and integrated them from the surface down to 100 meters depth, along the section shown in Figure 7a. The energy conversion terms were averaged over 10 days prior to the date indicated in Figure 7a. The magnitude of the vertical buoyancy flux (VBF) prevailed over the two other terms (i.e., HRS and VRS; see Figure 7b (top)). Near the coast, the horizontal shear of the flow is intense compared to offshore, and the potential vorticity is close to zero. This indicates a conversion of mean kinetic energy to eddy kinetic energy via horizontal shear instability along the coast. There VBF is negative, whereas it is positive offshore. The vertical section of the Ertel potential vorticity shows vertical changes of its horizontal gradient. This a necessary condition for baroclinic instability to occur (see Figure 7b (bottom)). The resulting submesoscale eddy is intense ($\zeta/f_0 \sim -1$) and its radius is about 30 km (see Figure 7c). Note that VBF changes sign along the section meaning that eddy potential energy is converted into eddy kinetic energy in some other places. Though their magnitudes are small compared to VBF, HRS, and VRS are negative along the section which indicates a conversion of mean kinetic to eddy kinetic energy. Note that EPV multiplied by the Coriolis parameter is negative in a thin layer over the sloping topography, possibly due to vertical mixing. Nonlinear advection terms are likely responsible for the high relative vorticity below this layer. The vertical section of the velocity component normal to the section (figure 7c), and the density contours, indicate that the submesoscale anticyclone is confined in the surface mixed layer, here the upper 40–50 m of the ocean.

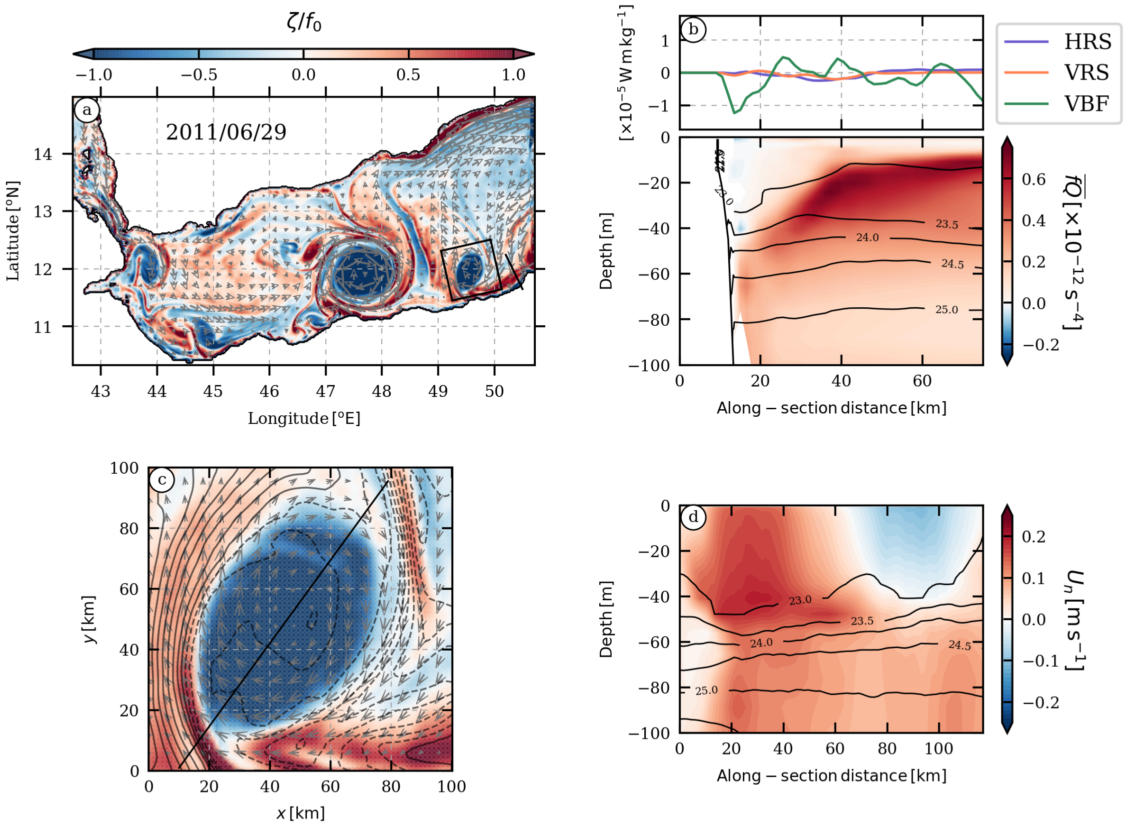

Figure 7. (**a**) Instantaneous surface vertical relative vorticity normalized by the areal average of the Coriolis frequency (f_0) in the Gulf of Aden. (**b**, **top**) Energy conversion terms integrated from the surface down to 100 m depth, and timely averaged over the 10 days before the date indicated in (**a**): horizontal Reynolds stress (HRS, in blue), vertical Reynolds stress (VRS, in orange), and vertical buoyancy flux (VBF, in green) in the along-section direction (see solid black line in (**a**) for location). (**b**, **bottom**) Vertical slice of the potential vorticity (Q) multiplied by the Coriolis frequency (f) (see solid black line in (**a**) for location) timely averaged over the 10 days before the date indicated in (**a**). Density contours are represented as solid black lines. (**c**) Zoom in the Gulf of Aden (see black squared box in (**a**) for location) over a submesoscale anticyclone near the southern coast. (**d**) Vertical slice of the normal velocity (see solid black line in (**c**) for location). Density contours are represented as solid black lines).

In the Gulf of Oman, intense submesoscale filaments are generated at the Cape of Ra's al Hamra and at the Cape of Ra's al Hadd in February, as shown in Figure 8a. The high relative vorticity ($\zeta/f_0 \sim 1$) indicates a strong horizontal shear of the structure. The generation of this submesoscale filament is associated with mean flow interaction with the topography, and detachment from the cape. The submesoscale filaments are also associated with a density front in the upper layer, as shown by the density contours in Figure 8b (bottom). This filament undergoes instabilities, the energy sources of which are the horizontal velocity shear and the vertical buoyancy flux, HRS and VBF, which are of the same order of magnitude, and which prevail on VRS. Thus, the submesoscale eddy generated downstream cape emanates from a mixed barotropic/baroclinic instability. Indeed, baroclinic instability of the filament can be related to its frontal structure, and barotropic instability to the gulf-scaled flow interaction with the sloping topography near the coast. The vertical section of the Ertel potential vorticity corroborates this result. The EPV gradient changes sign vertically near the surface while horizontal changes in sign of the EPV gradient occur below. The unstable submesoscale filaments generate a street of submesoscale cyclonic eddies which merge and form the cyclone shown in Figure 8c. The resulting cyclone is 25 km in radius and has a deep dynamical influence (see Figure 8d). The cross-section component of the horizontal velocity decreases gradually down to about 1000 m. The velocity of the submesoscale cyclone is intensified in the upper 300 m of the gulf.

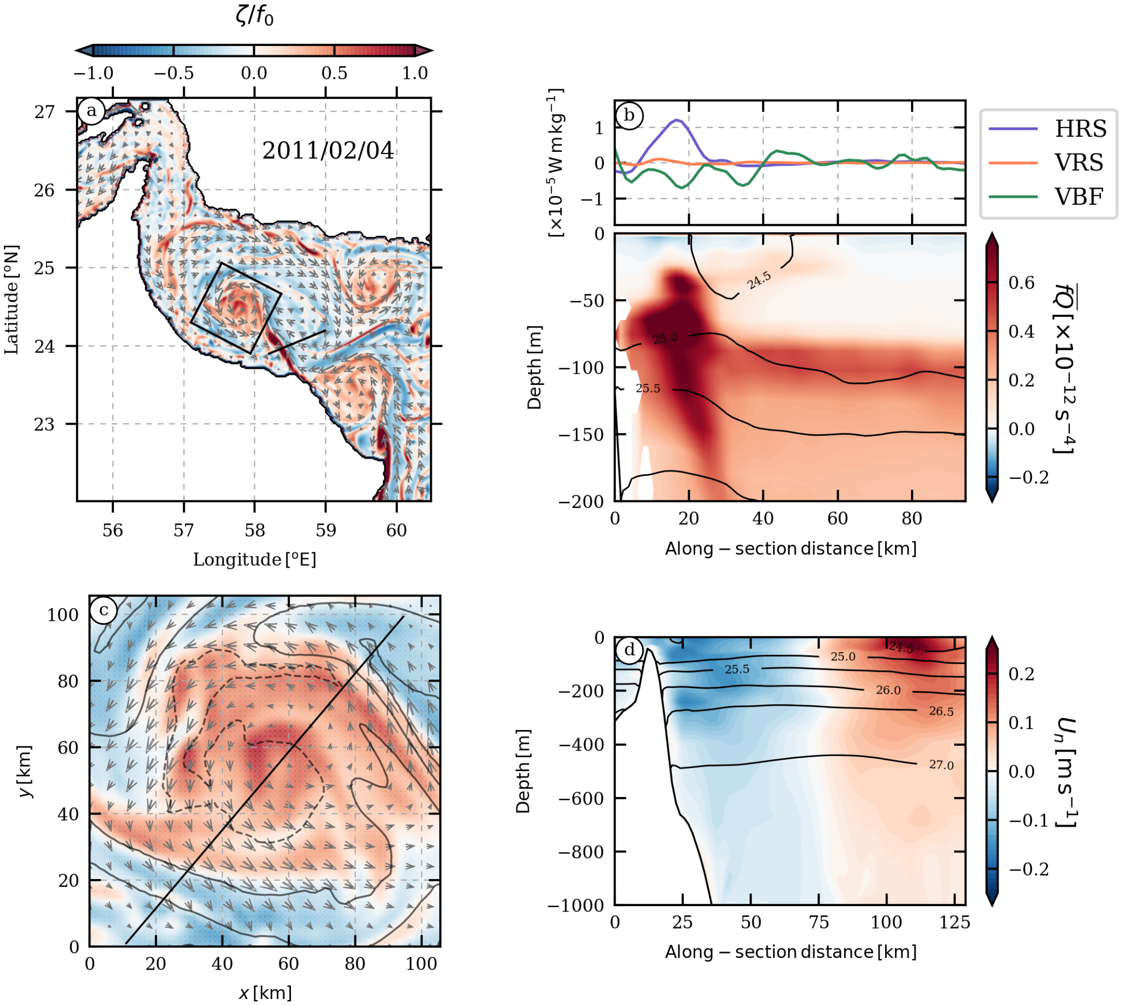

Figure 8. (**a**) Instantaneous surface vertical relative vorticity normalized by the areal average of the Coriolis frequency (f_0) in the Gulf of Oman. (**b**, **top**) Energy conversion terms integrated from the surface down to 100 m depth, and timely averaged over the 10 days before the date indicated in (**a**): horizontal Reynolds stress (HRS, in blue), vertical Reynolds stress (VRS, in orange), and vertical buoyancy flux (VBF, in green) in the along-section direction (see solid black line in (**a**) for location). (**b**, **bottom**) Vertical slice of the potential vorticity (Q) multiplied by the Coriolis frequency (f) (see solid black line in (**a**) for location) timely averaged over the 10 days before the date indicated in (**a**). Density contours are represented as solid black lines. (**c**) Zoom in the Gulf of Oman (see black squared box in (**a**) for location) over a submesoscale anticyclone near the southern coast. (**d**) Vertical slice of the normal velocity (see solid black line in (**c**) for location). Density contours are represented as solid black lines).

3.4. Deep Influences of Submesoscale Structures

As mentioned in Section 1, the mesoscale eddies often drive the circulation in the Gulf of Oman and the Gulf of Aden. The velocity field associated with these eddies can reach 1000 m depth. Therefore, mesoscale eddies represent a large part of the barotropic component of the flow field in both gulfs. In figure 9, we show the distribution of the enstrophy in the two-dimensional (k,m) Fourier space, where k and m are respectively the isotropic horizontal and vertical wave numbers. The enstrophy spectra show the strong barotropic component ($m \leq 5 \times 10^{-3}$ cpm) of the flow at larger scale ($k \leq R_d^1$). This is the signature of the above-mentioned mesoscale eddies. Below the deformation radius, the submesoscale enstrophy spectra are different depending on the gulf considered. In the Gulf Oman, we identified a peak centered at $k \sim 1 \times 10^{-1}$ cpkm and $m \sim 1 \times 10^{-2}$ cpm. In the Gulf of Aden, the enstrophy spectrum exhibits two peaks. The first one is centered at the scale of the deformation radius, the second one at $k \sim 1 \times 10^{-1}$ cpkm. The vertical wave number associated with these two peaks is $m \sim 1 \times 10^{-2}$ cpm. The Gulf of Oman has more enstrophy at basin scale (related to the cyclonic circulation at gulf scale in winter) and the Gulf of Aden shows a distinct peak at submesoscale, related to the eddies that we have described earlier.

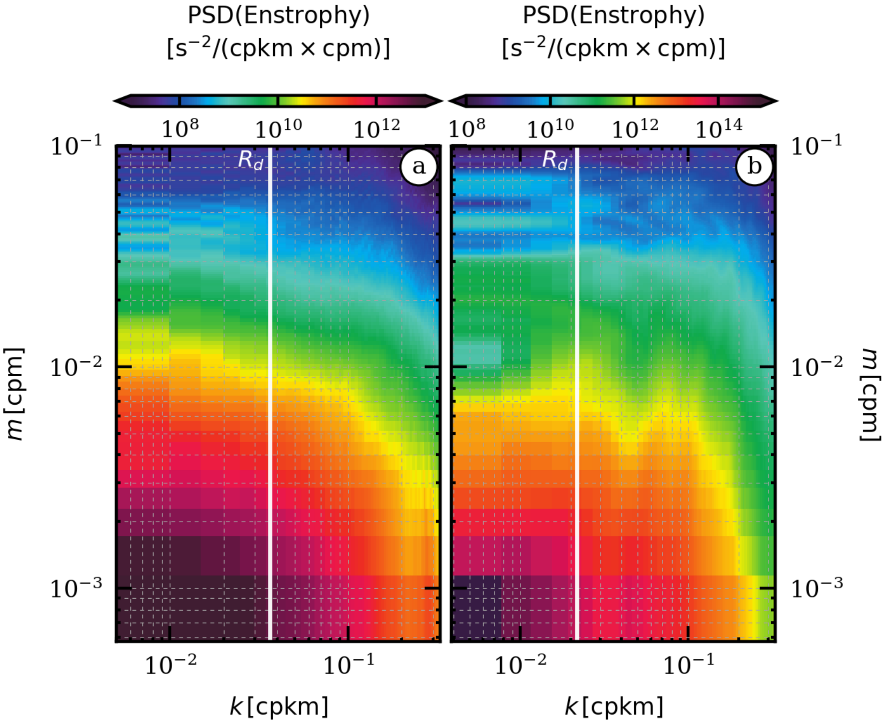

Figure 9. Power Spectrum Densities (PSDs) of enstrophy computed (**a**) in the Gulf of Oman, and (**b**) in the Gulf of Aden. The deformation radius is indicated in vertical solid white lines.

3.5. Subsurface Submesoscale Eddies

RSW and PGW spread at intermediate depth respectively in the Gulf of Oman and the Gulf of Aden.

RSW stabilizes on the 27.0 kg m^{-3} isopycnal between 400 and 800 m depth. We show an instantaneous view of the salinity on this isopycnic surface in Figure 10a. The RSW flows out of the Red Sea following the southern coast of the Gulf of Aden. As this outflow reaches the Cape of Berbera, submesoscale eddies are generated. Upstream of the cape, the vertical buoyancy flux prevails on the horizontal and vertical Reynolds stress, for the energy transfers, as shown in Figure 10b (top). Therefore, the RSW outflow is baroclinically unstable. The salinity maximum is found at 400 m depth on the 27.0 kg m^{-3} isopycnal. The salty water vein extends from 200 down to 1000 m depth (see Figure 10b (bottom)). Downstream of the cape, a dipolar vortex is generated. The relative vorticity of the cyclonic part of this dipole is shown in Figure 10c. It has a complex structure. Indeed, the cyclone (anticyclone) results from the merger of submesoscale eddies successively generated at the cape. The vertical section of the cross component of the velocity (see Figure 10d) shows that the cyclone velocity is indeed intensified deeper than those of anticyclones usually found in the gulf, i.e., here at about 550 m depth. This is also a clue that baroclinic instability occurs, as heton like eddies are formed, in agreement with the idealized experiments described in [28]. The radius of the submesoscale cyclone is about 15 km and its vertical extent is about 400 m.

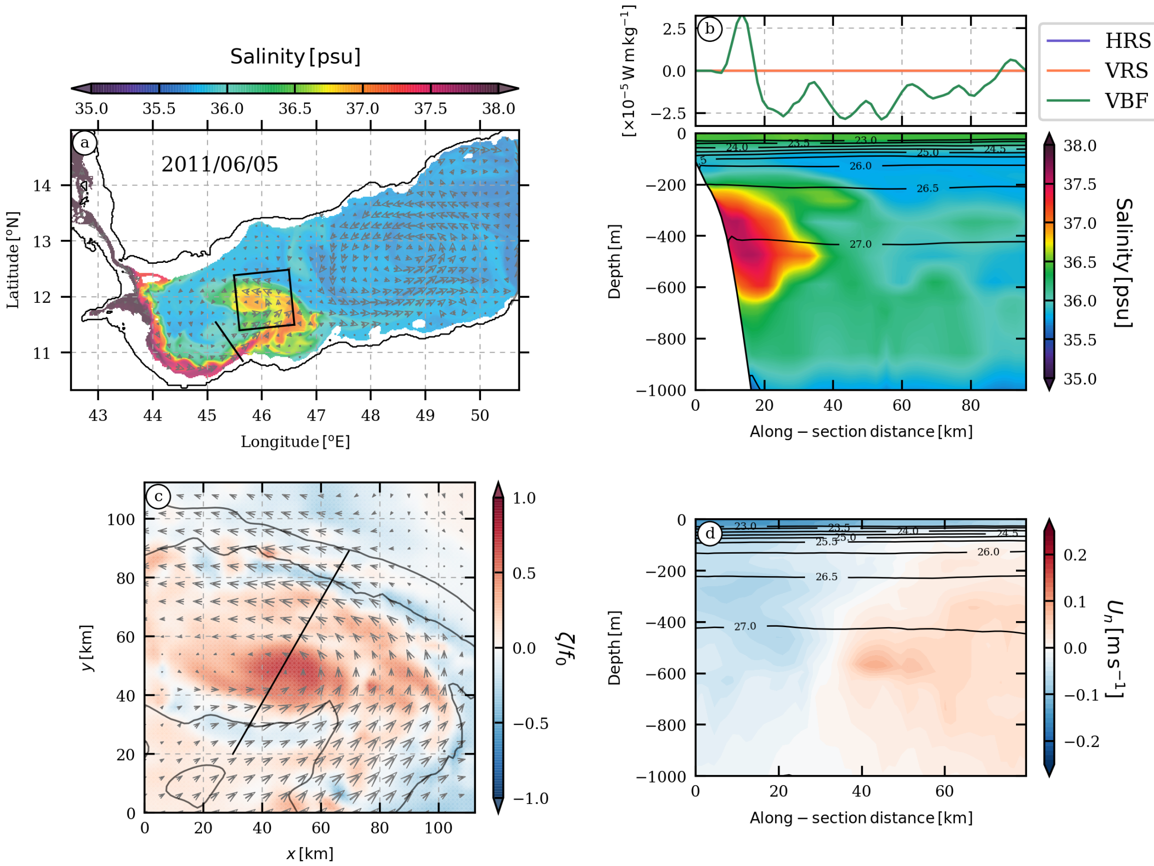

Figure 10. (**a**) Instantaneous salinity interpolated on the $\sigma_0 = 27.0\,\mathrm{kg\,m^{-3}}$ density level in the Gulf of Aden. Arrows stand for the velocity vectors interpolated on the same density level. (**b**, **top**) Energy conversion terms integrated from the surface down to 100 m depth, and timely averaged over 20 days centered at the date indicated in (**a**): horizontal Reynolds stress (HRS, in blue), vertical Reynolds stress (VRS, in orange), and vertical buoyancy flux (VBF, in green) in the along-section direction (see solid black line in (**a**) for location). (**b**, **bottom**) Vertical slice of salinity (see solid black line in (**a**) for location). Density contours are represented as solid black lines. (**c**) Zoom in the Gulf of Aden (see black squared box in (**a**) for location) over a submesoscale anticyclone near the southern coast. Vertical relative vorticity normalized by the Coriolis frequency averaged over the region (f_0) interpolated on the $\sigma_0 = 27.0\,\mathrm{kg\,m^{-3}}$ density level. Arrows stand for the velocity vectors interpolated on the same density level. (**d**) Vertical slice of the normal velocity (see solid black line in (**c**) for location). Density contours are represented as solid black lines).

In the Gulf of Oman, PGW stabilizes on the $26.5\,\mathrm{kg\,m^{-3}}$ isopycnic level between 150 and 300 m depth. The salinity interpolated on this isopycnic surface is shown in Figure 11a. At the Cape of Ra's al Hamra, submesoscale eddies of PGW are generated. Indeed, upstream of the cape, the PGW outflow is baroclinically unstable since the vertical buoyancy flux is larger than the horizontal and the vertical shear production (see Figure 10b (top). Conversion from eddy potential to eddy kinetic energy thus accompanies the formation of submesoscale eddies. The salty PGW vein extends from 150 down to 300 m depth as shown in Figure 11b (bottom). Now, we zoom on one submesoscale anticyclone (see Figure 11c). Its relative vorticity is less intense (in norm) than that of the submesoscale eddy found in the Gulf of Aden, and described above. Two successively generated submesoscale eddies of PGW can be observed along the Omani coast. Thus the baroclinic instability of the PGW outflow is long lasting, and the PGW outflow can generate several submesoscale eddies. But, contrary to those in the Gulf of Aden, submesoscale eddies do not interact with each other and merge, here. They drift along the Omani coast. Thus the advecting current due to the mesoscale eddies is fast enough to separate them. This can be related to the high energy found at mesoscale in the spectra (shown above).

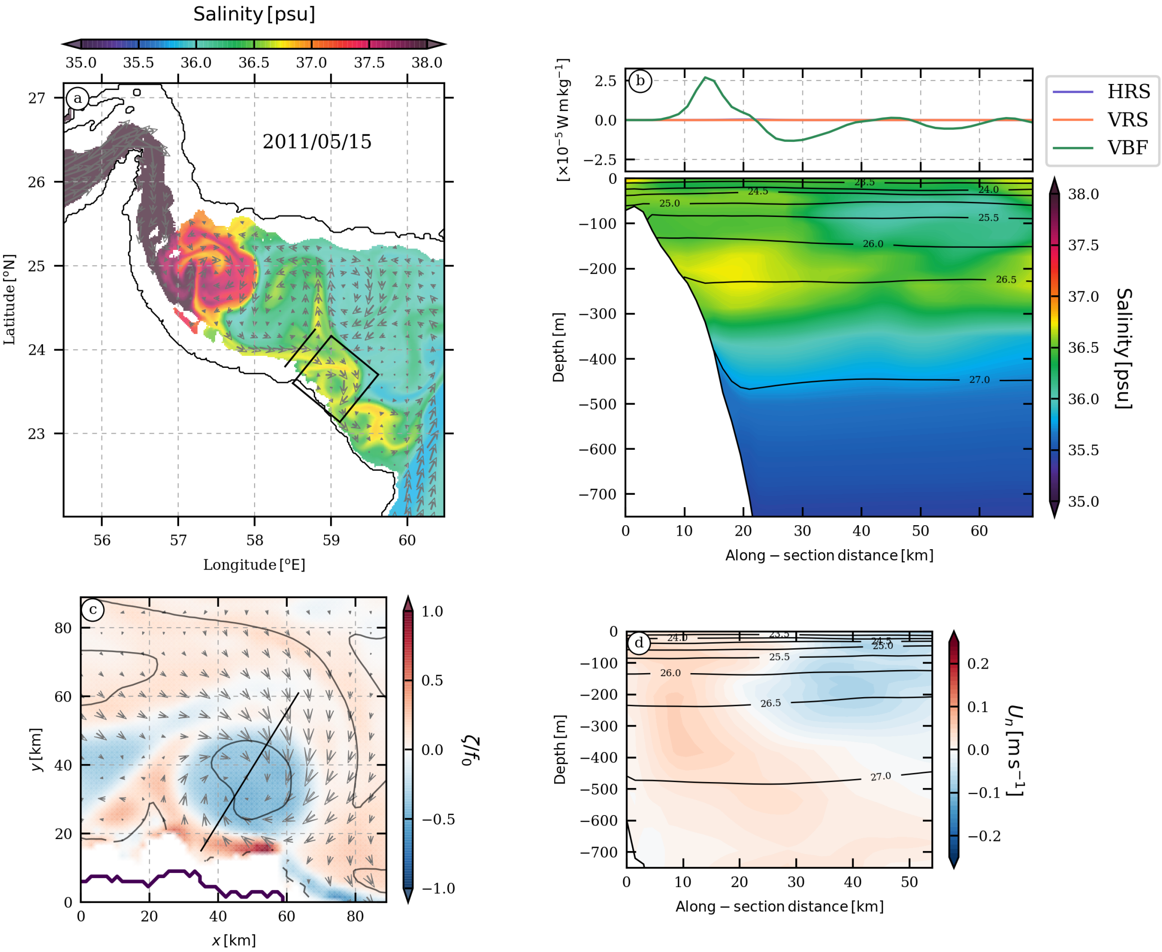

Figure 11. (**a**) Instantaneous salinity interpolated on the $\sigma_0 = 26.5\,\mathrm{kg\,m^{-3}}$ density level in the Gulf of Oman. Arrows stand for the velocity vectors interpolated on the same density level. (**b**, **top**) Energy conversion terms integrated from the surface down to 100 m depth, and timely averaged over 20 days centered at the date indicated in (**a**): horizontal Reynolds stress (HRS, in blue), vertical Reynolds stress (VRS, in orange), and vertical buoyancy flux (VBF, in green) in the along-section direction (see solid black line in (**a**) for location). (**b**, **bottom**) Vertical slice of salinity (see solid black line in (**a**) for location). Density contours are represented as solid black lines. (**c**) Zoom in the Gulf of Oman (see black squared box in (**a**) for location) over a submesoscale anticyclone near the southern coast. Vertical relative vorticity normalized by the Coriolis frequency averaged over the region (f_0) interpolated on the $\sigma_0 = 26.5\,\mathrm{kg\,m^{-3}}$ density level. Arrows stand for the velocity vectors interpolated on the same density level. (**d**) Vertical slice of the normal velocity (see solid black line in (**c**) for location). Density contours are represented as solid black lines).

This rapid advection could also explain the observation of a lens of PGW south-east of Ras al Hadd, by [18] at the same period of year 2011. This small anticyclone had certainly been advected around a mesoscale surface anticyclone, since the lens had thermohaline characteristics of PGW at Ras al Hamra (far upstream of Ras al Hadd).

Here, from the vertical section of the cross component of the horizontal velocity (see Figure 11d), the radius of this submesoscale eddy is about 15 km and the vertical extent of the submesoscale anticyclone is about 200 m.

The submesoscale eddy production has implications on the spreading and diffusion of RSW and PGW. The distributions of salinity in the one-dimensional (k) Fourier space, upstream and downstream of the capes, are shown in Figure 12. By comparing the slopes at meso- and submesoscale, it results that the flattest spectra appear downstream of the capes. This reflects an active submesoscale eddy field there, driving the fate of PGW and RSW. The horizontal maps of salinity interpolated on the neutral density in the Gulf of Aden and the Gulf of Oman (see respectively Figure 10a and Figure 11a) show that RSW and PGW are transported by submesoscale eddies. We also compare the T/S diagram upstream and downstream of the capes in Figure 13. Upstream of the cape, the highest salinity value of RSW (PGW) is about 38 (39) psu. Downstream of the cape, RSW (PGW) has mixed with the surrounding water masses. The maximal value of RSW (PGW) reduces to 36 (37) psu.

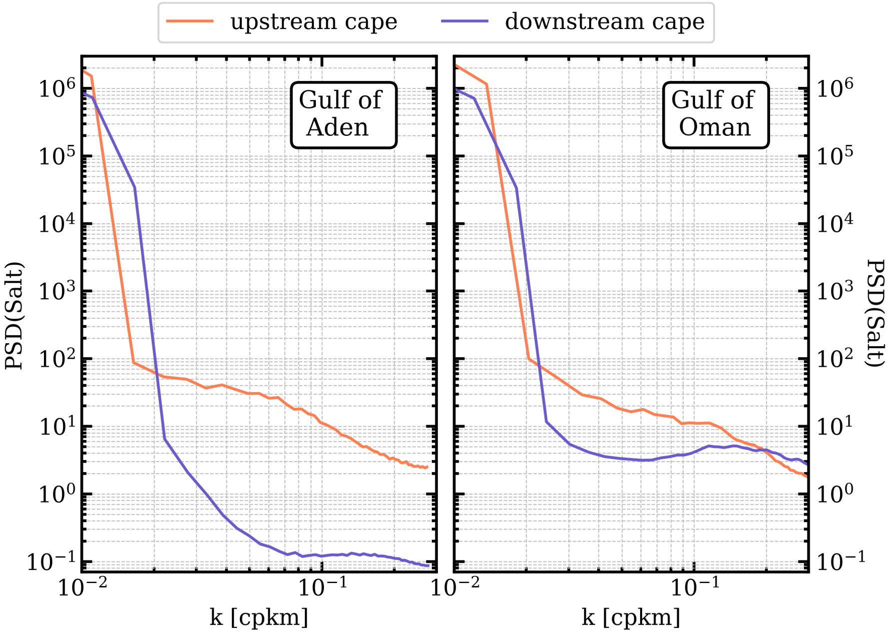

Figure 12. Power Spectral Densities of salinity (**left**) in the Gulf of Aden and (**right**) in the Gulf of Oman, (orange) upstream and (blue) downstream of the capes.

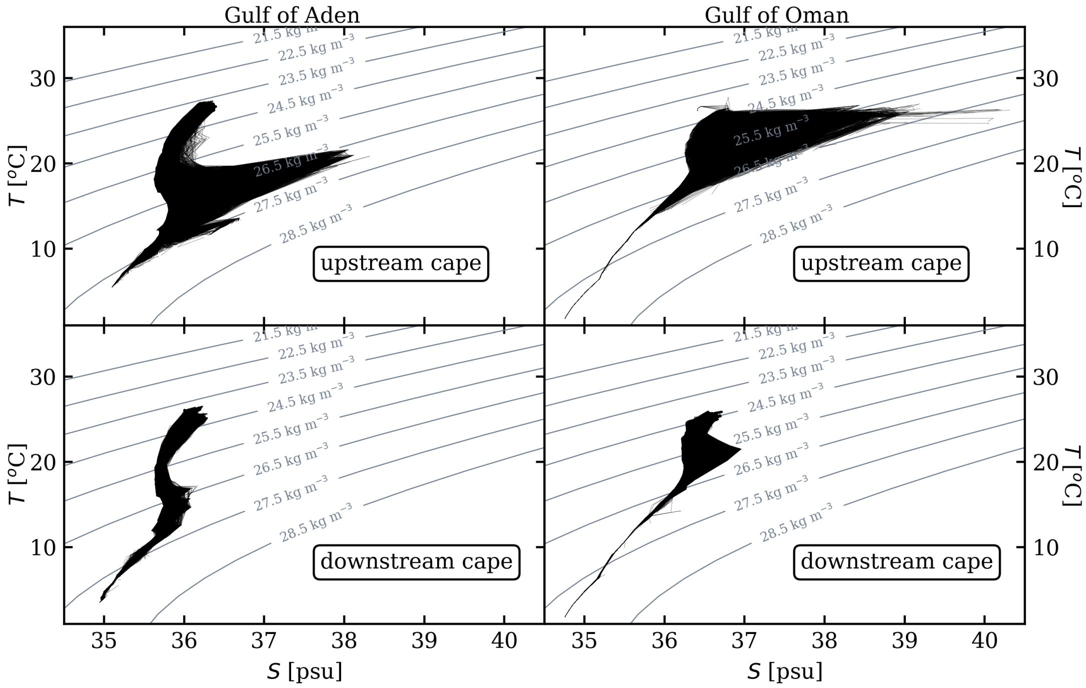

Figure 13. T/S diagram (**left**) in the Gulf of Aden and (**right**) in the Gulf of Oman, (**top**) upstream and (**bottom**) downstream of the cape. Density contours are drawn as solid gray lines.

4. Summary and Conclusions

This paper has focused on the submesoscale dynamics both at the surface and subsurface in the Gulf of Aden and in the Gulf of Oman by analysing outputs of regional numerical simulations performed with a primitive equation model at submesoscale resolution. The dynamics in the gulfs have been identified as the interactions of mesoscale and submesoscale eddies and filaments, fronts instabilities, and fast waves.

We have shown that submesoscale eddies and filaments are the results of several physical phenomena, such as local upwelling systems and coastal current instabilities at the surface, and baroclinic instability at capes subsurface. In the Gulf of Oman, submesoscale eddies appear near Ras al Hamra and Ras al Hadd but mesoscale eddies prevail. In the Gulf of Aden, submesoscale eddies are formed near the Cape of Berbera and via the shear instability of upwelling filaments. The presence of these small eddies is reflected by flatter slopes of energy (or enstrophy) spectra. These spectra clearly help identify the horizontal and vertical scales of both mesoscale and submesoscale eddies which are seen also in horizontal maps of vertical relative vorticity and in temperature or salinity maps. The 3D structure of these small eddies was also presented from the model results.

Spectra also helped identify the different waves in the two gulfs: The rotational spectra had the signature of long baroclinic Rossby waves which advect mesoscale eddies westward in the Gulf of Aden. The divergent spectrum is marked by the internal Kelvin waves, the inertia-gravity waves, and the tidal waves.

Finally, the subsurface submesoscale eddies formed at capes impact the RSW and the PGW by carrying and then mixing these salty waters with surrounding water masses. The correlation between salinity and vorticity peaks at the level of the outflows is clearly seen in isopycnic maps. The temperature–salinity diagrams for upstream and downstream of the capes where these small eddies form also show the enhanced diffusion of heat and salt at these locations.

This paper has provided a first glimpse at submesocale dynamics in these two gulfs. Still, a finer resolution model would be necessary to fully grasp the richness of submesocale dynamics in this region. Many questions are also left open: How do surface and sub-surface submesoscale features interact? Can the submesoscale lenses of RSW escape the Gulf of Aden and reach the longitude where a few of them were observed in the early 1980s? Conversely, can submesoscale surface eddies, formed in the Arabian Sea, enter these gulfs, and participate in the larger-scale conversion of water masses, to which the lenses of PGW or of RSW contribute? Indeed, it is known that the marginal seas convert fresher inflows into salty outflows. Previously, it was thought that these inflows and outflows contained only coastal and slope currents and mesoscale eddies. This study opens the door to a non negligible role of submesoscale features in this specific large-scale exchange. This contribution remains to be quantified more precisely. Finally, what are the roles of these submesoscale eddies and filaments in the regional marine biology and biogeochemistry? These questions are left for further studies.

Author Contributions: X.C., S.C., and R.B. designed the numerical experiments. S.C. and R.B. performed the numerical experiments. M.M. obtained and analyzed the results. M.M. and X.C. wrote the manuscript. All authors have read and agreed to the published version of the manuscript.

Funding: This research received no external funding.

Acknowledgments: MM was supported by a contract from SHOM "Validation du modele HYCOM sur la mer d'Arabie"; this work was done in partial fullfilment of the requirements for his PhD in physical oceanography.

Conflicts of Interest: The authors declare no conflict of interest.

References

1. Bowser, A.S.; Hunt, H.D.; Price, J.F. Character and dynamics of the Red Sea and Persian Gulf outflows. *J. Geophys. Res. Oceans* **2000**, *105*, 6387–6414.
2. Pous, S.; Carton, X.; Lazure, P. Hydrology and circulation in the Strait of Hormuz and the Gulf of Oman—Results from the GOGP99 Experiment: 2. Gulf of Oman. *J. Geophys. Res. Oceans* **2004**, *109*, doi:10.1029/2003JC002146.
3. Bower, A.S.; Johns, W.E.; Fratantoni, D.M.; Peters, H. Equilibration and circulation of Red Sea Outflow Water in the western Gulf of Aden. *J. Phys. Oceanogr.* **2005**, *35*, 1963–1985.
4. Carton, X.; L'Hegaret, P.; Baraille, R. Mesoscale variability of water masses in the Arabian Sea as revealed by ARGO floats. *Ocean Sci.* **2012**, *8*, 227–248.
5. Bower, A.S.; Furey, H.H. Mesoscale eddies in the Gulf of Aden and their impact on the spreading of Red Sea Outflow Water. *Prog. Oceanogr.* **2012**, *96*, 14–39.
6. Carton, X. Hydrodynamical modeling of oceanic vortices. *Surv. Geophys.* **2001**, *22*, 179–263.
7. de Marez, C.; Meunier, T.; Morvan, M.; L'Hégaret, P.; Carton, X. Study of the stability of a large realistic cyclonic eddy. *Ocean Model.* **2020**, *146*, 101540.
8. Al Saafani, M.; Shenoi, S.; Shankar, D.; Aparna, M.; Kurian, J.; Durand, F.; Vinayachandran, P. Westward movement of eddies into the Gulf of Aden from the Arabian Sea. *J. Geophys. Res. Oceans* **2007**, *112*, doi:10.1029/2006JC004020.
9. L'Hégaret, P.; Lacour, L.; Carton, X.; Roullet, G.; Baraille, R.; Corréard, S. A seasonal dipolar eddy near Ras Al Hamra (Sea of Oman). *Ocean Dyn.* **2013**, *63*, 633–659.
10. Chelton, D.B.; Deszoeke, R.A.; Schlax, M.G.; El Naggar, K.; Siwertz, N. Geographical variability of the first baroclinic Rossby radius of deformation. *J. Phys. Oceanogr.* **1998**, *28*, 433–460.
11. Vic, C.; Roullet, G.; Capet, X.; Carton, X.; Molemaker, M.J.; Gula, J. Eddy-topography interactions and the fate of the Persian Gulf Outflow. *J. Geophys. Res. Oceans* **2015**, *120*, 6700–6717.
12. Vic, C.; Capet, X.; Roullet, G.; Carton, X. Western boundary upwelling dynamics off Oman. *Ocean Dyn.* **2017**, *67*, 585–595.
13. McWilliams, J.C. Submesoscale, coherent vortices in the ocean. *Rev. Geophys.* **1985**, *23*, 165–182.
14. D'Asaro, E.A. Generation of submesoscale vortices: A new mechanism. *J. Geophys. Res. Oceans* **1988**, *93*, 6685–6693.
15. Bosse, A.; Testor, P.; Mortier, L.; Prieur, L.; Taillandier, V.; d'Ortenzio, F.; Coppola, L. Spreading of Levantine Intermediate Waters by submesoscale coherent vortices in the northwestern Mediterranean Sea as observed with gliders. *J. Geophys. Res. Oceans* **2015**, *120*, 1599–1622.

16. Collins, C.A.; Margolina, T.; Rago, T.A.; Ivanov, L. Looping RAFOS floats in the California current system. *Deep. Sea Res. Part II Top. Stud. Oceanogr.* **2013**, *85*, 42–61.
17. Gula, J.; Blacic, T.M.; Todd, R.E. Submesoscale coherent vortices in the Gulf Stream. *Geophys. Res. Lett.* **2019**, *46*, 2704–2714.
18. L'Hégaret, P.; Carton, X.; Louazel, S.; Boutin, G. Mesoscale eddies and submesoscale structures of Persian Gulf Water off the Omani coast in spring 2011. *Ocean Sci.* **2016**, *12*, 687–701.
19. Shapiro, G.; Meschanov, S. Distribution and spreading of Red Sea Water and salt lens formation in the northwest Indian Ocean. *Deep. Sea Res. Part A Oceanogr. Res. Pap.* **1991**, *38*, 21–34.
20. Meschanov, S.; Shapiro, G. A young lens of Red Sea Water in the Arabian Sea. *Deep. Sea Res. Part I Oceanogr. Res. Pap.* **1998**, *45*, 1–13.
21. de Marez, C.; Carton, X.; Corréard, S.; L'Hégaret, P.; Morvan, M. Observations of a deep submesoscale cyclonic vortex in the Arabian Sea. *Geophys. Res. Lett.* **2020**, *47*, e2020GL087881.
22. Capet, X.; McWilliams, J.C.; Molemaker, M.J.; Shchepetkin, A. Mesoscale to submesoscale transition in the California Current System. Part I: Flow structure, eddy flux, and observational tests. *J. Phys. Oceanogr.* **2008**, *38*, 29–43.
23. Capet, X.; McWilliams, J.C.; Molemaker, M.J.; Shchepetkin, A. Mesoscale to submesoscale transition in the California Current System. Part II: Frontal processes. *J. Phys. Oceanogr.* **2008**, *38*, 44–64.
24. Capet, X.; McWilliams, J.C.; Molemaker, M.J.; Shchepetkin, A. Mesoscale to submesoscale transition in the California Current System. Part III: Energy balance and flux. *J. Phys. Oceanogr.* **2008**, *38*, 2256–2269.
25. Molemaker, M.J.; McWilliams, J.C.; Dewar, W.K. Submesoscale instability and generation of mesoscale anticyclones near a separation of the California Undercurrent. *J. Phys. Oceanogr.* **2015**, *45*, 613–629.
26. Gula, J.; Molemaker, M.J.; McWilliams, J.C. Submesoscale dynamics of a Gulf Stream frontal eddy in the South Atlantic Bight. *J. Phys. Oceanogr.* **2016**, *46*, 305–325.
27. Morvan, M.; L'Hégaret, P.; Carton, X.; Gula, J.; Vic, C.; Marez, C.d.; Sokolovskiy, M.; Koshel, K. The life cycle of submesoscale eddies generated by topographic interactions. *Ocean Sci.* **2019**, *15*, 1531–1543.
28. Morvan, M.; Carton, X.; L'Hégaret, P.; de Marez, C.; Corréard, S.; Laouzel, S. On the dynamics of an idealized bottom density current overflowing in a semi-enclosed basin: Mesoscale and submesoscale eddies generation. *Geophys. Astrophys. Fluid Dyn.* **2020**, doi:10.1080/03091929.2020.1747058.
29. McWilliams, J.C. Submesoscale currents in the ocean. *Proc. R. Soc. A Math. Phys. Eng. Sci.* **2016**, *472*, 20160117.
30. Chassignet, E.P.; Hurlburt, H.E.; Smedstad, O.M.; Halliwell, G.R.; Hogan, P.J.; Wallcraft, A.J.; Baraille, R.; Bleck, R. The HYCOM (hybrid coordinate ocean model) data assimilative system. *J. Mar. Syst.* **2007**, *65*, 60–83.
31. Debreu, L.; Vouland, C.; Blayo, E. AGRIF: Adaptive grid refinement in Fortran. *Comput. Geosci.* **2008**, *34*, 8–13.
32. Morvan, M.; L'Hégaret, P.; de Marez, C.; Carton, X.; Corréard, S.; Baraille, R. Life cycle of mesoscale eddies in the Gulf of Aden. *Geophys. Astrophys. Fluid Dyn.* **2020**, 1–19, doi:10.1080/03091929.2019.1708348.
33. Large, W.G.; McWilliams, J.C.; Doney, S.C. Oceanic vertical mixing: A review and a model with a nonlocal boundary layer parameterization. *Rev. Geophys.* **1994**, *32*, 363–403.
34. Haynes, P.; McIntyre, M. On the conservation and impermeability theorems for potential vorticity. *J. Atmos. Sci.* **1990**, *47*, 2021–2031.
35. Gula, J.; Molemaker, M.J.; McWilliams, J.C. Topographic generation of submesoscale centrifugal instability and energy dissipation. *Nat. Commun.* **2016**, *7*, 12811.
36. L'Hégaret, P.; Duarte, R.; Carton, X.; Vic, C.; Ciani, D.; Baraille, R.; Corréard, S. Mesoscale variability in the Arabian Sea from HYCOM model results and observations: Impact on the Persian Gulf Water path. *Ocean Sci.* **2015**, *11*, 667.
37. Torres, H.S.; Klein, P.; Menemenlis, D.; Qiu, B.; Su, Z.; Wang, J.; Chen, S.; Fu, L.L. Partitioning ocean motions into balanced motions and internal gravity waves: A modeling study in anticipation of future space missions. *J. Geophys. Res. Oceans* **2018**, *123*, 8084–8105.

38. Torres, H.; Klein, P.; Siegelman, L.; Qiu, B.; Chen, S.; Ubelmann, C.; Wang, J.; Menemenlis, D.; Fu, L.L. Diagnosing ocean-wave-turbulence interactions from space. *Geophys. Res. Lett.* **2019**, *46*, 8933–8942.
39. Hoskins, B. The role of potential vorticity in symmetric stability and instability. *Q. J. R. Meteorol. Soc.* **1974**, *100*, 480–482.